Energy Technology
Generation, Conversion, Storage, Distribution
www.entechnol.de

Non-Uniform Chemical Corrosion of Metal Electrode of p–i–n Type of Perovskite Solar Cells Caused by the Diffusion of CH_3NH_3I

Shuxuan Guo, Xue Sun, Changzeng Ding, Rong Huang, Mingxi Tan, Lanping Zhang, Qun Luo, Fangsen Li, Jing Jin, and Chang-Qi Ma**

Although perovskite solar cells have shown high power conversion efficiency, performance stability is still insufficient. Herein, the decay kinetics of the p–i–n type of perovskite cells under light illumination is monitored. It is found that the degradation of the performance is mainly caused by the decrease in short-circuit current (J_{SC}), which is directly related to the loss of active area. Secondary ion mass spectrometry (SIMS) analysis confirms that both $CH_3NH_3^+$ and I^- migrate toward the metal electrode during aging through the thin $PC_{61}BM$ layer. Atomic force microscope (AFM) and scanning electron microscope (SEM) analyses reveal that some part of the $PC_{61}BM$ layer is too thin to cover the rough surface of the perovskite film fully. Therefore, chemical corrosion of the metal electrode by CH_3NH_3I leads to the loss of active area and the consequent short circuit current is proposed to be the performance decay mechanism of perovskite solar cells, which is further supported by the stability improvement of the cells by inserting a thin bathocuproine (BCP) buffer layer between the metal electrode and $PC_{61}BM$, where the CH_3NH_3I migration is blocked by the BCP layer.

1. Introduction

Organic–inorganic hybrid perovskite materials have become the most intriguing semiconductor for use in photovoltaics owing to their excellent photoelectric properties, such as solution processability, high absorption coefficient, high charge mobility, and long charge diffusion length and low exciton binding energy.[1] As Miyasaka et al. reported the first perovskite solar cells (PSCs) in 2009,[2] the power conversion efficiency (PCE) of perovskite solar cells has rocketed from the initial 3.8% to the current 25.2%[3] in only 10 years. Various device structures, including mesoporous type,[4] n–i–p-type planar[5] and p–i–n type-planar cells[6,7] have been developed. Among these, the p–i–n type cells have the advantages of low processing temperature, low hysteresis,[8] high performance at low operation temperature,[6] and are considered as a good candidate for space applications.[9–11]

Over the last decade, most of the research works are focusing on improving the efficiency of the cells through material development and device structure optimization.[1,12] To realize the commercialization of perovskite solar cells, an urgent problem that needs to be solved is to improve their stability, as the operation lifetime of the perovskite solar cell is still far from satisfactory.[13,14] Understanding the degradation mechanism of the perovskite solar cells is the first step to solve the degradation problem. Up to now, different degradation processes have been clarified in the literature, including the decomposition of perovskite films caused by water,[15,16] oxygen,[17] thermal heating,[18,19] or phase transition of the perovskite crystalline films,[18] ions aggregations,[20] and ions migrations.[21–25] In general, the degradation process caused by water and/or oxygen can be suppressed by introducing a hydrophobic interlayer[26–29] or proper encapsulation,[30] and these can be considered as extrinsic degradation processes. However, the degradation processes owing to the phase transition or ions migration of the perovsktie film cannot be suppressed by thin film encapsulation, and are considered as the intrinsic degradation process that is the most critical issue for the stability improvement of perovskite solar cells.

Perovskite is a typical ionic crystal semiconductor, and the ion migration behaviors of this material are significant, which will

S. Guo, Prof. J. Jin
School of Material Science and Engineering
Shanghai University
99 Shangda Road, Shanghai 200444, P. R. China
E-mail: jjin@shu.edu.cn

S. Guo, X. Sun, C. Ding, M. Tan, L. Zhang, Prof. Q. Luo, Prof. C.-Q. Ma
Printable Electronics Research Center
Suzhou Institute of Nano-Tech and Nano-Bionics
Chinese Academy of Sciences (CAS)
Suzhou 215123, P. R. China
E-mail: cqma2011@sinano.ac.cn

Prof. R. Huang, Prof. F. Li
Vacuum Interconnected Nanotech Workstation
Suzhou Institute of Nano-Tech and Nano-Bionics
Chinese Academy of Sciences (CAS)
Suzhou 215123, P. R. China

Prof. Q. Luo, Prof. C.-Q. Ma
Suzhou Institute of Nano-Tech and Nano-Bionics Nanchang
Chinese Academy of Sciences (CAS)
298 Luozhu Road, Nanchang 330200, P. R. China

The ORCID identification number(s) for the author(s) of this article can be found under https://doi.org/10.1002/ente.202000250.

DOI: 10.1002/ente.202000250

bring a great threat to the stability of perovskite solar cells. Abate et al.[21] provided direct evidence of halogen and cation migration within perovskite layers by elemental depth profiling and modeling, respectively, which will lead to the hysteresis and reversible decay of the cells. In addition to the ion migration within the perovskite film, ion migration between perovskite and electrode modification layers was found to be serious that causes performance decay. For example, Yang et al. demonstrated that halogen ions would cross the entire [6,6]-phenyl-C_{61}-butyric acid methyl ester ($PC_{61}BM$) layer and react with the metal electrode resulting in damage to the metal electrode and the electrode interface.[24] Fang et al. demonstrate that halogen atoms can penetrate through the $PC_{61}BM$ layer under light illumination, thermal heating, or electric filed driving, which led to performance decay.[23] Furthermore, diffusion of metal atoms through the perovskite also reported,[31,32] which are also considered as one of the main reasons for the degradation of perovskite solar cells. As for the driving force for ion migration, it was reported that electric bias and light are the two most important factors.[32–34] However, how the halogen ions migrate toward the metal electrode and what the counter $CH_3NH_3^+$ ions behave during irreversible degradation are still not fully understood yet.

In this article, we systematically studied the decay kinetics of the p–i–n type perovskite solar cells with a structure of ITO/PEDOT:PSS/$MAPbI_3$/$PC_{61}BM$/Al (PEDOT:PSS: poly(3,4-ethylenedioxythiophene):poly(styrene sulfonate)) under the operating conditions. Results revealed that the performance decay of this type of cells was mainly due to the fast decay of short-circuit current (J_{SC}), which originally comes from the non-uniform damage of the metal electrode. By using time-of-flight secondary ion mass spectrometry (ToF-SIMS), we confirmed the migration of both $CH_3NH_3^+$ and I^- toward the metal electrode during aging. In the meanwhile, diffusion of Al^{3+} toward the perovskite film was also found. Based on these findings, a chemical corrosion of metal electrode by the diffusion of CH_3NH_3I was proposed. Detailed discussion on the driving force for the migration of CH_3NH_3I and method to suppress the degradation is provided in this article.

2. Results and Discussion

2.1. Decay Kinetics of the Cells

A set of 16 pieces (altogether 64 cells) of p–i–n cells with a structure of ITO/PEDOT:PSS (≈35 nm)/$MAPbI_3$ (≈250 nm)/$PC_{61}BM$ (≈60 nm)/Al (100 nm) were fabricated accordingly to the procedure we previously developed.[35] The current density–voltage (J–V) characteristic of the best cell and the histogram of the efficiency of 64 cells are shown in **Figure 1**a,b, respectively. The external quantum efficiency (EQE) spectrum of the best cell and the averaged device performance data are shown in Figure S1 and Table S1, Supporting Information, respectively. As seen here, the best cell showed a PCE of 16.06% with an open-circuit (V_{OC}) of 1.01 V, a short-circuit current (J_{SC}) of 19.88 mA cm^{-2} (corresponding reasonably well with the integrated J_{SC} calculated from EQE spectrum which is 21.18 mA cm^{-2}; Figure S1, Supporting Information), and FF of 0.80, and most of the cells show PCE of 15.0–15.5% and an averaged PCE of 15.14%, which is comparable to the literature reported PCE for the same device structure,[36] indicating the device are well optimized and suitable for stability comparison.

First, we compared the shelf and operation stability of these cells. Figure 1c shows the performance evolutions of the devices under dark storage or light illumination condition. As seen here, the perovskite solar cells showed reasonably good stability under dark storage, and PCE can maintain about 60% of its initial device performance after 1300 h, which is consistent with that reported by Lee.[37] In contrast, device performance decayed very fast when the cell was aged at operation condition (under light illumination with external load to match the maximum power point [mpp]). After being aged for about 200 h, PCE of the device has been reduced to less than 20% of the initial value, indicating that light illumination causes the fast performance degradation. On the contrary, from the perspective of the degradation parameters of the device, we found that J_{SC} dominates the overall performance decay, whereas V_{OC} and FF are rather stable during aging (less than 10% decay).

2.2. Correlation the J_{SC} Decay to the Loss of Effective Area

The appearance of the aged cells is shown in Figure S2, Supporting Information. Clearly, defects on the electrode can be seen for the light-aged cell, whereas the electrode surface is almost complete and homogenous for the shelf-aged cell. We then measured the surface morphology of the metal electrode by optical microscope, and checked the photocurrent distribution of the cell using a laser-beam-induced current (LBIC) imaging method, where a small laser beam (with a diameter of 10 μm) to illuminate the cell and the photo current is recorded by a source meter (see Figure S3, Supporting Information, for the measuring setup). The obtained images are shown in **Figure 2** and Figure S4, Supporting Information, for the light-aged and shelf-aged cells, respectively. For the pristine cell, few visible spots can be seen in the optical images (a2 in Figure 2). As the measured photocurrent is homogeneously distributed over the entire device area as seen from the LBIC image (a1 in Figure 2), these spots seen in the optical images are then ascribed to the dust on the electrode or surface defects that are not harmful to the device performance. After aged for 15 h under light illumination, more defects can be clearly seen from the LBIC image (b1) and optical image (b2). Note that defects are randomly distributed within the device area; the formation of defects cannot be due to the penetration of H_2O and/or O_2 from the edge of the electrode. We also found that the distribution of defects in the optical image corresponds well to the LBIC low current sites, suggesting that the J_{SC} decay is directly correlated to the defect on the electrode. With the increase in aging time, larger defects area and lower photocurrents were measured in some specific area (c and d series in Figure 2), indicating the growth of defects during aging. It worth pointing out that high photocurrent area can still be measured for the cell aged for 36 and 57 h (the red area in c1 and d1), indicating that degradation of the cell is spatially inhomogeneous and some parts of the cell are still working well. In contrast, defect growth is much slower for the cell aged in the dark (Figure S3, Supporting Information), corresponding well to the degradation kinetics of this type of cells (Figure 1c).

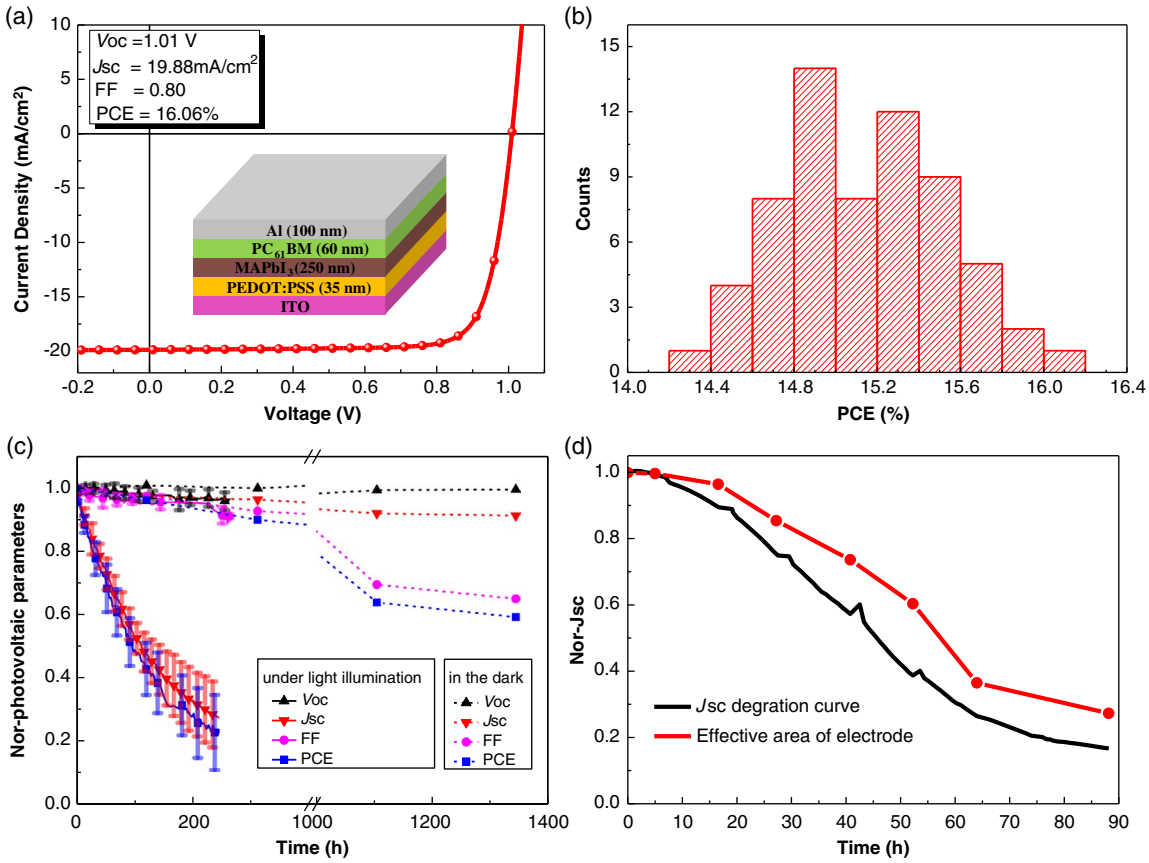

Figure 1. a) The device structure of the p-i-n type perovskite solar cells and the *J-V* curves of the best performance solar cell; b) histogram of efficiencies measured for 64 devices; c) the evolution of the perovskite solar cells aged in the dark at room temperature in a nitrogen atmosphere or at 45 ± 2 °C under 1 sun continuous illumination in a nitrogen atmosphere. Note that the aging time axis is broken from 400 to 1000 h; d) comparison of the J_{SC} decay and the loss of effective area under aging.

These results indicate that performance decay of this type of perovskite solar cell is more correlated to the defects on the top electrode rather than under the metal electrode.

To quantify the proportion of defects in the entire device area, we transfer the optical image to a black-and-white binary image using the open-source Image J.[38] The resulting images are shown in Figure 2 (a3–d3), where the defect region is indicated as black, and the effective region is indicated as white. The proportion of the defect area to the total area of the cell was then calculated and plotted against aging time (Figure 1d). Interestingly, we found that J_{SC} decay is in good consistency with the decrease in the effective area of the cell, indicating that electrode defect is the most important reason causing the J_{SC} decay. As the cells are aged in an inert atmosphere and the defect formation is not due to the penetration of H_2O and/or O_2 through the edge of the electrode (*vide supra*), such a performance decay is then recognized as an intrinsic process of this type of cell.

2.3. Ion Migrations within the Cell during Aging

We then performed ToF-SIMS measurements to check the element distribution of the cells to understand the ion migration behaviors within the cell. For comparison, we checked element depth profiles on regions both without any obvious defect (named intact region) and with surface defects (named defect region), in as shown **Figure 3**a,b, respectively. As shown in Figure 3a, relatively high mass spectra (MS) signals of CN^- and I^- were obtained over $PC_{61}BM$ layer even for the freshly prepared cell. Based on the fundamental components used in the perovskite solar cells, the measured CN^- and I^- signals probably have been come from CH_3NH_3I layer. The finding suggests that CH_3NH_3I will diffuse into the $PC_{61}BM$ layer during the preparation of cells. Moreover, a slight difference was observed between profiles of CN^- and I^-, where CN^- is almost constant over the whole $PC_{61}BM$ layer, whereas I^- is higher at the $PC_{61}BM$/perovskite interface. This may be due to a lower diffusion rate of I^- than $CH_3NH_3^+$, owing to the complex capability of I^- with $PC_{61}BM$ layer. Upon aging, no much difference was found of element profiles within perovskite layer in intact regions, suggesting that perovskite film does not degrade much under light illumination for some special area, which is also in good agreement with the high measured current in the LBIC image. Furthermore, higher CN^- and I^- signals were detected on the surface of the metal electrode, indicating that CH_3NH_3I further diffused through $PC_{61}BM$/Al layers and reached

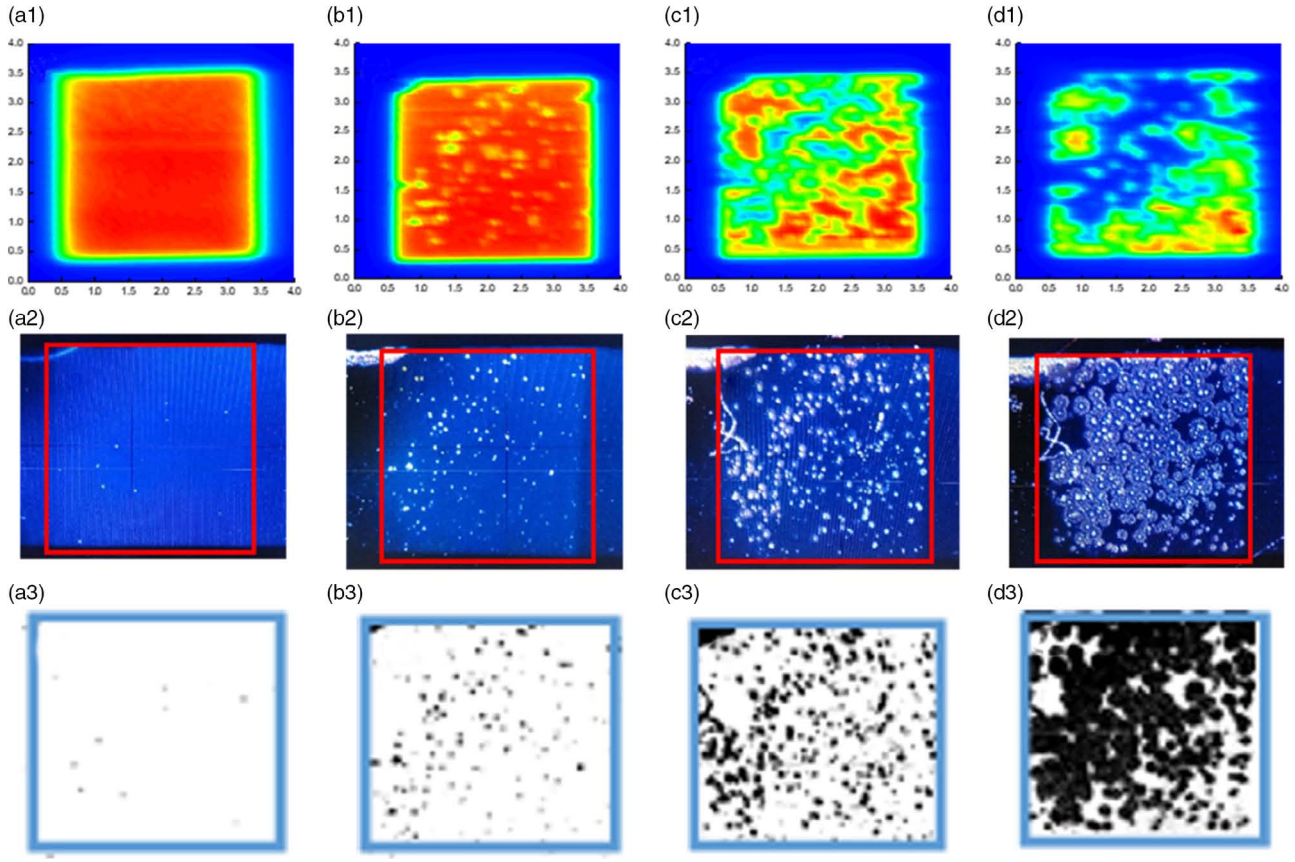

Figure 2. LBIC (a1–d1) and optical microscope (a2–d2) images for the a) pristine, b) aged 15 h, c) aged 36 h and d) aged 57 h cells. The cells aged under 1 sun continuous illumination in a nitrogen atmosphere at 45 ± 2 °C. The corresponding binary images obtained from the optical microscope images are shown in a3–d3, and the square framework indicates the device area with a dimension of 3 mm × 3 mm.

the metal electrode surfaces. Also, the accumulation of I at $PC_{61}BM$/Al interface was detected, which might be due to the formation of AlI_3 at the $PC_{61}BM$/Al interface.

In defect region, on the contrary, two to three orders of magnitude increase of CN^- and I^- signals were presented over entire Al/$PC_{61}BM$ layers upon aging (Figure 3b), and high Al signal intensity was also measured within the perovskite film. As the determination of each layer is based on a comprehensive consideration of the distribution of various elements such as Pb, C, In Al, and so on (see Figure S5, Supporting Information), rather than just relying on the results of the freshly prepared sample, the broadening of the distribution of I, CN, and Al elements could not be attributed the formation of pinholes during aging,[32,39] but to the ion migrations. In other words, the SIMIS results indicate that large amounts of CH_3NH_3I penetrated through $PC_{61}BM$ and reaches aluminum layers, whereas Al^{3+} ions diffuse through the $PC_{61}BM$ and get inside the perovskite films. Knowing that CH_3NH_3I is highly acidic, the measured Al^{3+} should be due to the chemical reaction of Al with $CH_3NH_3^+$ which includes the following two steps:

the oxidation of aluminum

$$Al \rightarrow Al^{3+} \quad (1)$$

the reduction of methylammonium anion

$$2CH_3NH_3^+ \rightarrow 2CH_3NH_2 \uparrow + H_2 \uparrow \quad (2)$$

and the overall reaction of

$$6CH_3NH_3I + 2Al \rightarrow 6CH_3NH_2 \uparrow + 2AlI_3 + 3H_2 \uparrow \quad (3)$$

Together with the decomposition of perovskite film, the overall decomposition of the perovskite solar cell owing to the chemical corrosion of aluminum electrode can be described as following

$$6CH_3NH_3PbI_3 + 2Al \rightarrow 6PbI_2 + 2AlI_3 + 6CH_3NH_2 \uparrow + 3H_2 \uparrow \quad (4)$$

Figure 4a shows the optical image of the electrode surface aged for 10 h, where volcano-like defects in a 50–100 μm scale can be clearly seen. ToF-SIMS surface imaging showed high I concentration on the defect area (Figure 4b), indicating that the main component on the defect is metal halide. Interestingly, no obvious CN signal was measured on the electrode surface (Figure 4c). We ascribed this to the high volatility of CH_3NH_2, which leaves the electrode surface after $CH_3NH_3^+$ is reduced (Equation (2)).

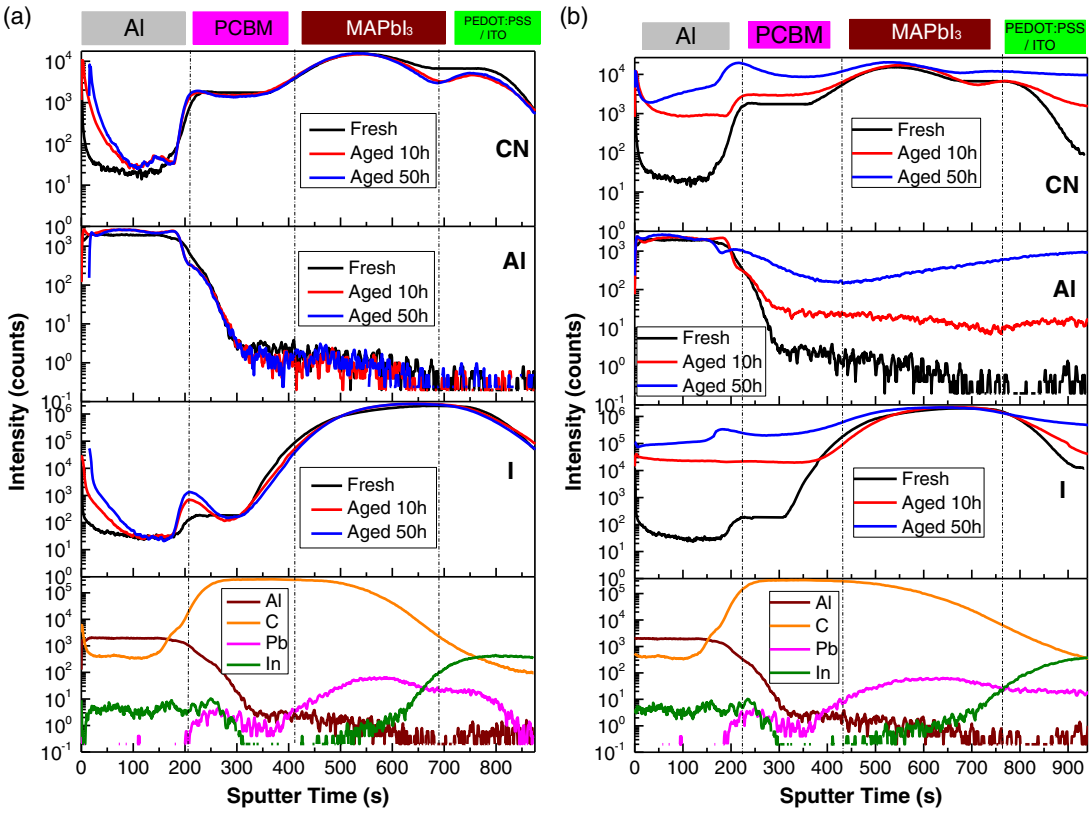

Figure 3. ToF-SIMS element profiles of the perovskite solar cells on the a) intact region and b) defect region. The layer boundaries are determined by the element distribution of Al, C, Pb, and In of a fresh cell.

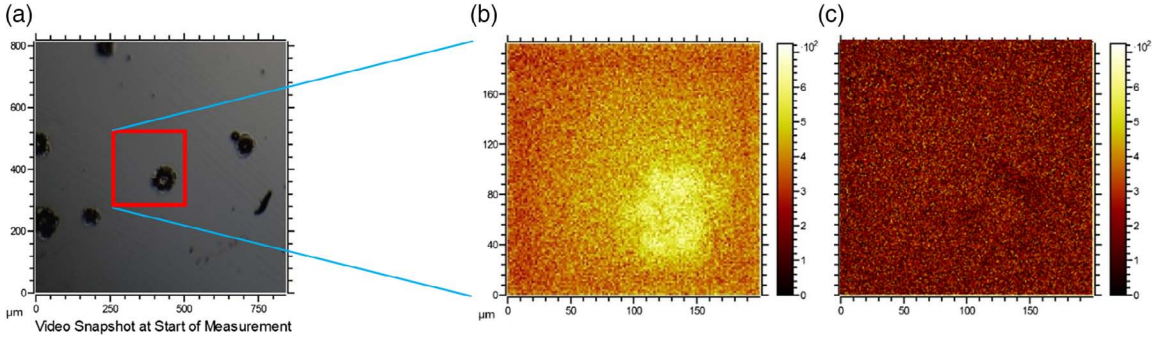

Figure 4. a) Optical photo image of the electrode surface of an aged cell and surface element distribution of element b) I and c) CN measured by ToF-SIMS. The devices aged at 45 ± 2 °C under 1 sun continuous illumination in a nitrogen atmosphere.

2.4. Surface Morphology of the $MAPbI_3$ and $MAPbI_3/PC_{61}BM$ Films

To further understand why the electrode corrosion happens non-uniformly upon aging, the surface morphology of the $MAPbI_3$ and $MAPbI_3/PC_{61}BM$ films were measured by atomic force microscope (AFM). **Figure 5**a,b show the AFM topological images of these two films. It can be seen that the $MAPbI_3$ film showed a very rough surface with a root-mean-surface roughness (RMS) of 17.8 nm, and the maximum peak-to-valley height of ≈120 nm, whereas the $MAPbI_3/PC_{61}BM$ film showed a smooth surface with an RMS of 3.4 nm and much smaller peak-to-valley height of ≈20 nm. Note that the layer thickness of the $PC_{61}BM$ film spin-coated from the same solution is around 60 nm. The rather smooth $MAPbI_3/PC_{61}BM$ surface indicates that the perovskite surface is not homogenously covered by the $PC_{61}BM$ layer, and some parts of the perovskite crystal peak might be covered by a very thin $PC_{61}BM$ film. To confirm this, the cross-sectional scanning electron microscopy (SEM) image of the freshly prepared perovskite solar cell was measured. As seen from **Figure 6**, the thickness of the $PC_{61}BM$ layer is not homogenous on top of perovskite film, and the thinnest spot

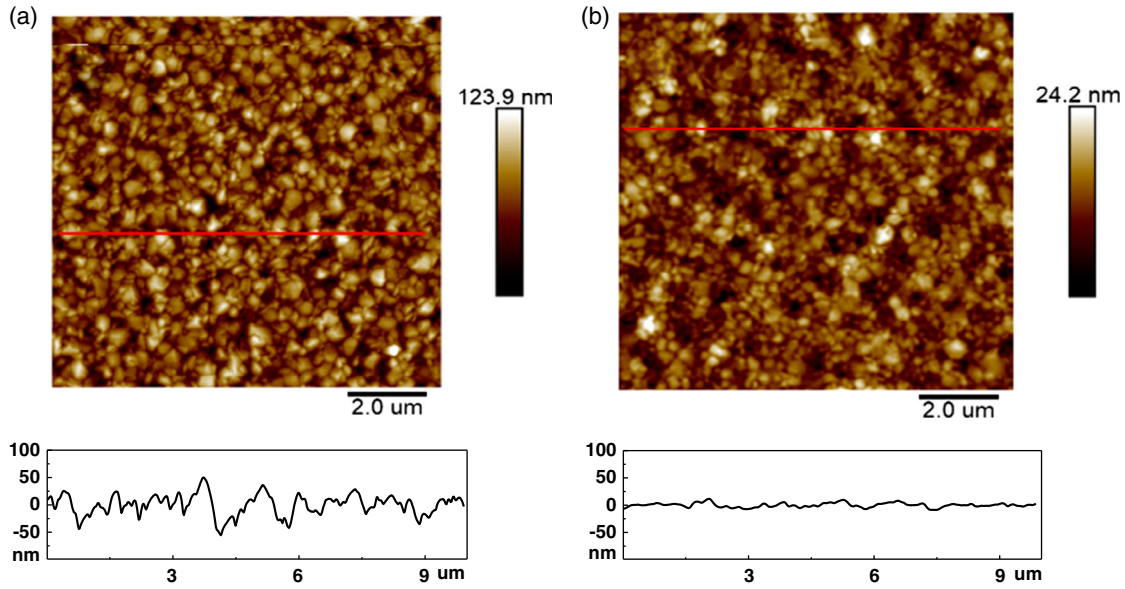

Figure 5. AFM topological images of a) $MAPbI_3$ b) $MAPbI_3/PC_{61}BM$. The 1D surface profile marked by the red line in the AFM images is placed under the AFM images.

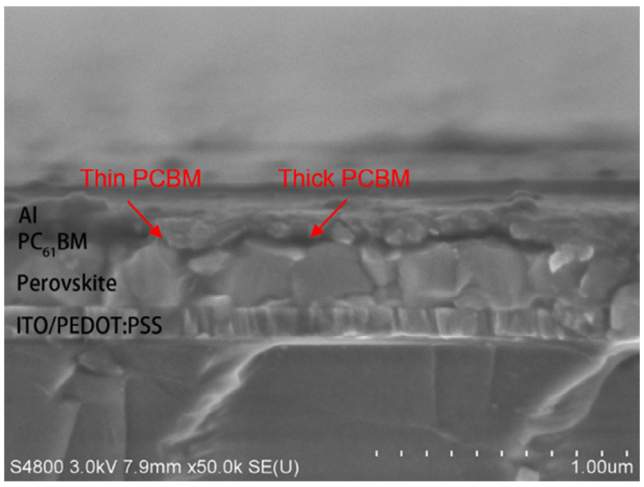

Figure 6. A cross-sectional SEM image of the fresh prepared perovskite solar cell showing that the thickness of the $PC_{61}BM$ layer is not homogenous on top of perovskite film.

of the $PC_{61}BM$ layer is difficult to be distinguished. Such a non-uniform coverage of the perovskite by $PC_{61}BM$ was also reported by other research groups,[26,40,41] which can be ascribed to the rough perovskite surface, as well as the low $PC_{61}BM$ layer thickness and the aggregation of $PC_{61}BM$. The thinnest $PC_{61}BM$ spots on the perovskite film become the most easily penetrated positions for halogen ions, which initiates the chemical corrosion of metal electrode. With the increase in the aging time, further corrosion of the electrode leads to the growth of apparent defects and reaching up to 100 μm, which are easily seen by optical microscope (Figure 2 and 4).

2.5. Light Driving Chemical Corrosion of Metal Electrode by CH_3NH_3I

As discussed at the very beginning, light illumination promotes the degradation of perovskite solar cells. Also, we tested the degradation kinetics of the perovskite cells aged at different load conditions, including short circuit, maximum power output point (mpp), and open-circuit conditions, and found that the cells decay much faster at open circuit than at short-circuit condition (Figure S6, Supporting Information), which is consistent with the previous reports.[33,42,43] These results indicate that both light illumination and external load are the key factors influencing the diffusion of CH_3NH_3I. Maier et al. reported orders of magnitudes enhancement of I^- migration within the perovskite film under light illumination (in both vertical and horizontal directions),[25] which was ascribed to the photon generated iodine vacancies within the perovskite film that relies on concentration of photon generated electron–hole pairs. Therefore, faster halogen ion migration is expected when the cell is illuminated at open-circuit condition because the higher concentration of the photogenerated electron-hole pairs formed at open-circuit condition, similar to that found in polymer solar cells.[44] However, this does not answer the question of the driving force for the ion migration toward the electrode. The SIMS results (Figure 3) of the cells in the defect region showed high CN and I concentration both in the top metal electrode and the bottom PEDOT:PSS layer, indicating that there is no preferential direction for CH_3NH_3I diffusion. Therefore, we attribute the ion migration behaviors to a concentration difference at different layers. Based on these, a chemical corrosion of aluminum electrode by the diffused CH_3NH_3I was proposed as shown in **Figure 7**, and the detailed chemical reactions involve the following key steps: 1) perovskite film decomposed to form CH_3NH_3I; 2) CH_3NH_3I diffused through the thinnest $PC_{61}BM$ region and

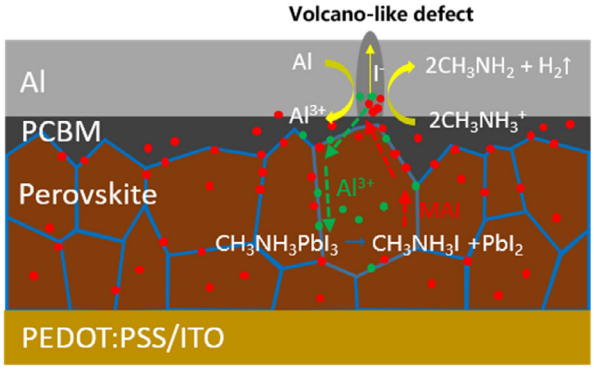

Figure 7. Proposed chemical corrosion of aluminum electrode of the p–i–n type perovskite solar cell by the diffusion of CH_3NH_3I.

reached the top metal electrode; 3) the CH_3NH_3I at the Al/$PC_{61}BM$ interface reacts with aluminum yielding AlI_3, CH_3NH_2, and H_2; 4) the generated H_2 gas will expand the electrode forming bubbles[40] on the electrode and eventually form volcano-like surface defects; 5) Al^{3+} ions diffuse into the perovskite layer causing the further decomposition of perovskite (Figure S7 Supporting Information), whereas the low CH_3NH_3I concentration at the Al/$PC_{61}BM$ enhances the diffusion of CH_3NH_3I toward the aluminum electrode to balance the chemical reaction.

2.6. Stability Improvement of the Cell by Inserting a Thin BCP Layer

Based on the degradation mechanism shown in Figure 7, we suppose that depositing an additional electron transporting layer on top $PC_{61}BM$ should be able to increase the distance between perovskite and metal electrode, which should be able to slow down the diffusion of CH_3NH_3I and consequently improve device stability. This concept has been proved by various interlayers, including ZnO,[41] TiO_2,[45] MoS_2,[46] and Cr_2O_3/Cr.[24] Bathocuproine (BCP; see **Figure 8**a for the chemical structure) as the most widely used hole blocking layer in OLED[47] has been used in perovskite solar cells as well for improving the device performance.[48,49] Chen et al. reported that device stability was improved by introducing a thin BCP layer owing to the hydrophobic property of the BCP layer.[49] However, there is no article discussing the effect of BCP on blocking ions diffusion in perovskite solar cells. We fabricated perovskite solar cells having an additional BCP layer on the top of $PC_{61}BM$, and checked the performance and stability of these cells. The layer thickness of BCP film was achieved by spin-coating BCP solution with different concentration. The *J–V* curves and EQE spectra of the champion devices with difference BCP layer thickness are shown in Figure 8c,d, respectively, and the photovoltaic data are shown in **Table 1**. In cooperation of a thin BCP layer increases the device performance slightly (15.33% vs 15.05%), which is similar to that reported in the literature and is ascribed to the improvement of

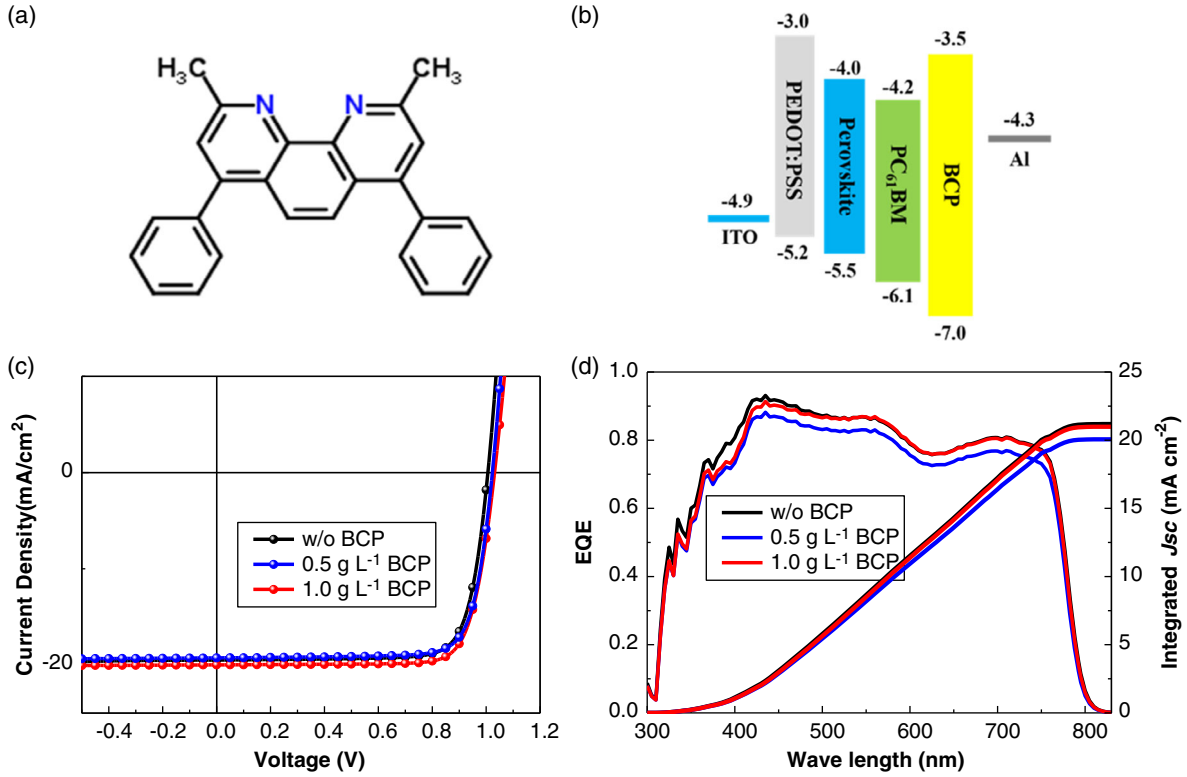

Figure 8. a) Chemical structure of BCP, b) energy-level diagram of the device, c) *J–V* curves, and d) EQE of the cells with different spin-coated from different BCP solution.

Table 1. Summary of photovoltaic parameters for devices with different concentration BCP.

Entry	BCP[a)]	V_{oc} [V]	J_{sc} [mA cm^{-2}]	FF	PCE [%]	T_{80}[b)]	η_{200}/η_0[c)]	PCE [∞][c)]	α[d)]	τ [h][d)]
1	w/o BCP	1.00 ± 0.01	19.36 ± 0.41	0.77 ± 0.01	15.05 ± 0.55	32 h	0.29	0.10	0.90	120
2	0.5 g L^{-1} BCP	0.98 ± 0.01	19.97 ± 0.12	0.77 ± 0.01	15.01 ± 0.21	40 h	0.43	0.33	0.65	169
3	1.0 g L^{-1} BCP	1.01 ± 0.01	19.83 ± 0.15	0.77 ± 0.01	15.33 ± 0.45	133 h	0.71	0.47	0.51	310
4	1.5 g L^{-1} BCP	0.99 ± 0.01	19.50 ± 0.09	0.77 ± 0.01	14.85 ± 0.24	–[e)]	–[e)]	–[d)]	–[d)]	–[d)]
5	2.0 g L^{-1} BCP	0.98 ± 0.02	19.66 ± 0.17	0.75 ± 0.01	14.49 ± 0.30	–[e)]	–[e)]	–[d)]	–[d)]	–[d)]

[a)]The concentration of BCP solution used for the preparation of BCP thin film; [b)]The time that reaches the 80% of its initial PCE; [c)]η_0: PCE of the cell before aging, η_{200}: PCE of the cell after aging for 200 h; [d)]Simulated numerical results obtained by fitting the PCE decay curves to the exponential decay model (Equation (5)); [e)]Not measured.

the contact between the ETL and the aluminum electrode by the BCP.[48,49] The EQE shapes (Figure 8d) of each cell are basically the same, indicating that the spin coating of the buffer layer has no effect on the perovskite active layer.

Figure 9 shows the evolution of photovoltaic parameters of the cells under light illumination. As seen here, the decline of J_{SC} in BCP based devices is significantly slower than the cells without BCP. T_{80}, the time that the cell reaches 80% of its initial PCE,[50] was measured to be 32, 40, and 133 h for the BCP-free, 0.5 and 1 g L^{-1} BCP-based cells, and the efficiency of the cell after aging for 200 h compared with its initial value (η_{200}) are 0.29, 0.43, and 0.71, respectively. To further quantitatively analyze the decay kinetics, the PCE decay curves were fitted using an exponential decay model as[51]

$$\mathrm{PCE}(t) = \mathrm{PCE}(\infty) + \alpha \times \exp\left(-\frac{t}{\tau}\right) \quad (5)$$

where τ, α, and PCE(∞) represent the mean lifetime, preexponential factor, and the intercept, respectively. The fitting curves are shown in Figure S8, Supporting Information, and the fitted parameters are shown in Table 1. As seen here, the mean lifetime τ is 120 h, 169 h, 310 h for the BCP-free, 0.5, and 1 g L^{-1} BCP-based cells, respectively. These results unambiguously confirming the stabilization effect of the BCP layer.

Huang et al. reported that accumulation of charge carrier at the interface would lead to fast performance decay in perovskite solar cells,[42] and thin BCP layer is able to increase the photocurrent by increase the electron injection efficiency,[48,49] this

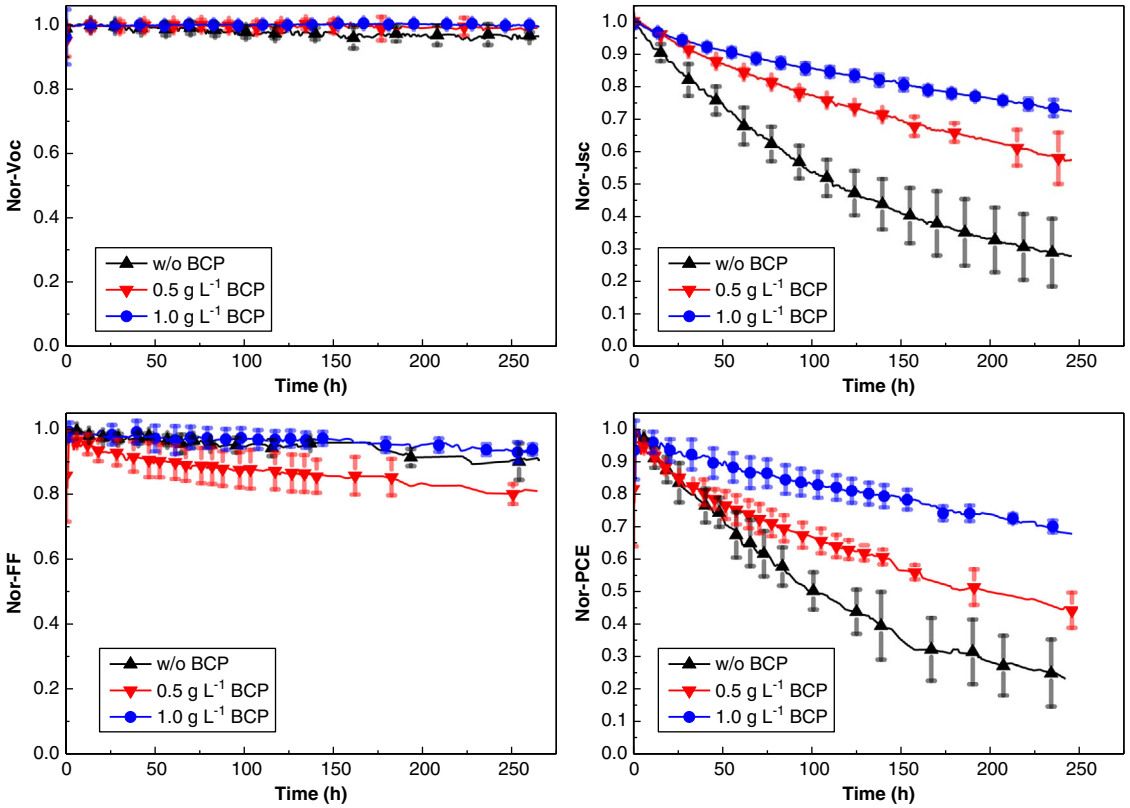

Figure 9. Evolution of photovoltaic parameters of the p–i–n cells with or without BCP interface with time. The cells were aged inside the glove box under 1 sun continuous illumination with a dynamic external load to meet the mpp point. The temperature of the cells was measured to be 45 ± 2 °C.

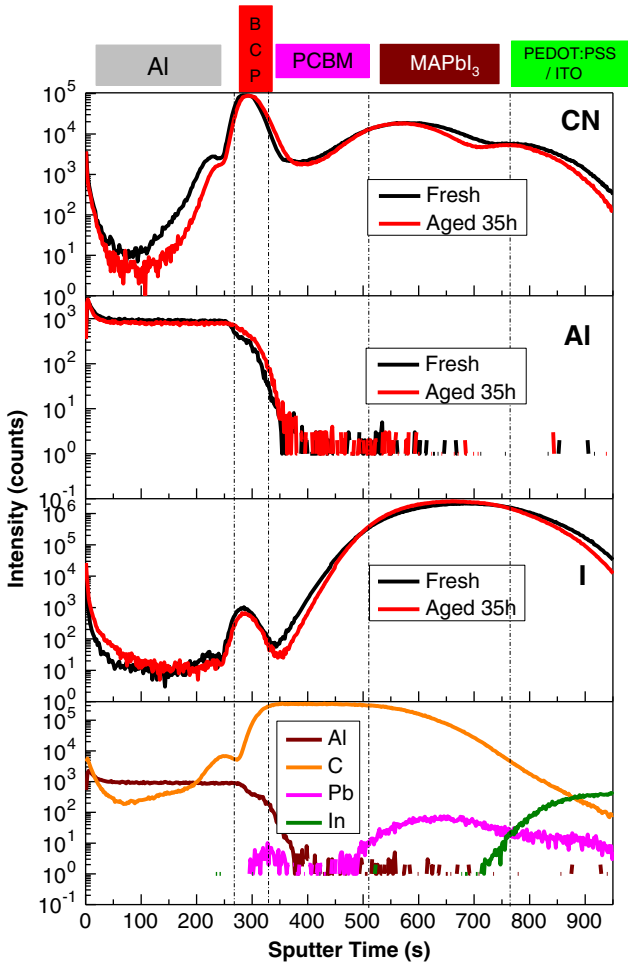

Figure 10. ToF-SIMS element profiles of the perovskite solar cells on the cell with BCP interfacial layer. The elements such as Al, C, Pb, and In depicted in the bottom graph is taken from the fresh cell.

could be one of the reasons for the stability improvement of BCP layer. Since CH_3NH_3I migration and the following chemical corrosion of metal electrode is proposed to be the main reason for the performance decay of perovskite solar cells, we performance SIMS measurements on the BCP based cells before and after aged for 35 h. **Figure 10** depicts the experiment result. The peak signal of the CN element can be clearly seen between the aluminum electrode and the ETL, indicating that BCP was successfully deposited on top of the $PC_{61}BM$ layer. By comparing the ToF-SIMS results of BCP devices before and after aging, we can see that the distribution of I and CN in the entire device is basically consistent, indicating that BCP does inhibit the migration of CH_3NH_3I. In addition, no visible electrode defect can be seen for the BCP coated cells (Figure S10, Supporting Information, confirming that the BCP layer is able to protect the aluminum electrode from the chemical corrosion by CH_3NH_3I.

3. Conclusion

In summary, we have systematically studied the degradation behaviors of the perovskite solar cells under operation conditions. By combining the detection of micro defects on the electrode and the changes of element distribution within the cell during aging, we confirmed that chemical corrosion of the aluminum electrode by the diffusion CH_3NH_3I is the main reason for the formation of defects on the aluminum electrode, which cause the loss of effective area and the consequent J_{SC} decay of the cell. The diffusion of CH_3NH_3I toward the metal electrode was attributed to the insufficient coverage of perovskite film by the $PC_{61}BM$ layer. Based on the understanding of the degradation mechanism, we establish an effective method to improve device stability by introducing an additional thin BCP layer, which on the one hand, proves the proposed degradation mechanism, on the other hand, provides an effective way to improve the stability of the perovskite solar cells.

4. Experimental Section

Materials: Poly(3,4-ethylenedioxythiophene):poly(styrene sulfonate) (PEDOT:PSS AI 4083) was purchased from Heraeus Precious Metals GmbH & Co. KG. $PbCl_2$ (99%), PbI_2 (99%), BCP (98%), and methylammonium iodide (MAI; 99.5%) were supplied by Xi'an Polymer Light Technology Corp. Phenyl-C_{61}-butyric acid methyl ester ($PC_{61}BM$) was purchased from Solenne B.V. All these materials were used as received without further purification.

Device Fabrication: The perovskite solar cells were fabricated according to the following procedure. Patterned indium tin oxide (ITO) substrates were cleaned with detergent aqueous solution, deionized water, acetone, and isopropanol, and finally ultraviolet-ozone (UVO) treating for 30 min. Then the PEDOT:PSS solution was spin-coated on the top of the cleaned ITO at 3500 rpm for 45 s and annealed at 130 °C for 10 min in the air. The other layers, including the perovskite layers, $PC_{61}BM$, and BCP layer were deposited inside the N_2 glove box. In detail, perovskite precursor solution was obtained by mixing CH_3NH_3I (103.35 mg), PbI_2 (306.56 mg), and $PbCl_2$ (9.73 mg) in DMSO/GBL solution (volume ratio 3:7) and stirred at 60 °C for 4 h. The precursor solution was spin-coated by a typical anti-solvent method at 1000 rpm for 10 s and 4000 rpm for 30 s. During spin-coating, chlorobenzene (CB) (400 µL) was quickly dropped onto the films with a delay time of 27 s after the beginning of the spin-coating. Then the substrate is annealed at 100 °C for 10 min to obtain perovskite films. After cooling to room temperature, the $PC_{61}BM$ solution (20 mg mL^{-1} in chlorobenzene) was spin-coated on the perovskite film at 1000 rpm for 60 s. BCP (1 mg mL^{-1} in ethanol) solution was spin-casted onto $PC_{61}BM$ at 4000 rpm for 15 s. Finally, a 100 nm Al layer was subsequently evaporated.

Characterization of Solar Cells: The current density–voltage (*J*–*V*) curves were measured in a nitrogen glove box with a Keithley 2400 source meter under simulated AM1.5G solar illumination (Verasol-2; 100 mW cm^{-2}, LED 3A Sun simulator, Newport). The photovoltaic performance data was obtained by the reverse scan from 1.2 to −0.5 V with a scan speed of 0.02 V s^{-1}. The EQE of each cell was measured using a home-made IPCE system consisting of a 150 W tungsten halogen lamp (Osram 64642), a monochromator (Zolix, Omni-l300), an optical chopper, and an I–V converter(QE-IV Convertor, Suzhou D&R Instruments) equipped with lock-in amplifier (Stanford Research Systems SR 830). To better simulate the device under 1 sun condition, bias light from a 532 nm solid-state laser was introduced to the cell simultaneously. A calibrated Si solar cell was used as a reference. The degradation kinetics of the unencapsulated perovskite solar cells was monitored by a decay testing system (PVLT-G8100M, Suzhou D&R Instruments) in a glove box ($H_2O < 10$ ppm, $O_2 < 10$ ppm) according to the condition of the ISOS-L-1I.[52] The cells were illuminated with white LED light (D&R Light, L-W5300KA-150, color temperature of 5300 K, Suzhou D&R Instruments). Light intensity was adjusted to meet the short-circuit current to simulate one sun aging condition. Owing to the light heating effect, the surface temperature of the device is around 45 ± 2 °C. The LBIC images were measured using a home-built microdefect detection system equipped with a laser

(532 nm) from a beam size of 10 μm, and an X–Y moving stage with a resolution of 0.5 μm. Surface photography was obtained by using an AFM (Dimension ICON) in the tapping mode. The cross section of perovskite solar cells were characterized by SEM (Hitachi S-4800). ToF-SIMS (IONTOF TOF.SIMS 5-100) was utilized for surface imaging and depth profile of perovskite solar cells. During depth profiling, sputtering ion beam (Cs^+ ion at 1 keV) was raster scanned over an area of $200 \times 200\ \mu m^2$. The analysis ion beam consisting of Bi^+ pulses (30 keV ion energy) was set in spectrometry mode and raster scanned over a $50 \times 50\ \mu m^2$ area centered within Cs^+ sputtered area. Image binarization was performed on a Java-based image conversion software Image J. Color image was imported into the ImageJ and then converted into 8-bit grayscale images with 256 grayscales. The threshold to define the boundary of black and white was set to a value that the defect region can be clearly seen and the noise cannot be seen in the complete electrode region. The ratio of dark area to the whole area was obtained directly from this software.

Supporting Information

Supporting Information is available from the Wiley Online Library or from the author.

Acknowledgements

The authors would like to acknowledge the financial support from the Ministry of Science and Technology of China (grant no. 2016YFA0200700), the National Natural Science Foundation of China (61904121), Chinese Academy of Science (grant no. YJKYYQ20180029, and CAS-ITRI 2019010), Natural Science Foundation of Jiangxi Province (20181BAB206017), Youth Innovation Promotion Association, CAS (2019317).

Conflict of Interest

The authors declare no conflict of interest.

Keywords

chemical corrosion, degradation mechanisms, ions migrations, perovskite solar cells, secondary ion mass spectrometry analysis

Received: March 17, 2020
Revised: May 2, 2020
Published online:

[1] M. I. H. Ansari, A. Qurashi, M. K. Nazeeruddin, *J. Photochem. Photobio. C* **2018**, *35*, 1.
[2] A T. K. S. Y. Kojima, T. Miyasaka, *J. Am. Chem. Soc.* **2009**, *131*, 6050.
[3] National Renewable Energy Laboratory, Best Research-Cell Efciencies, **2020**, https://www.nrel.gov/pv/assets/pdfs/best-research-cell-efficiencies.20200218.pdf, (accessed 03 March 2020).
[4] E. H. Jung, N. J. Jeon, E. Y. Park, C. S. Moon, T. J. Shin, T.-Y. Yang, J. H. Noh, J. Seo, *Nature* **2019**, *567*, 511.
[5] R. Wang, J. Xue, K.-L. Wang, Z.-K. Wang, Y. Luo, D. Fenning, G. Xu, S. Nuryyeva, T. Huang, Y. Zhao, J. L. Yang, J. Zhu, M. Wang, S. Tan, I. Yavuz, K. N. Houk, Y. Yang, *Science* **2019**, *366*, 1509.
[6] X. Zheng, Y. Hou, C. Bao, J. Yin, F. Yuan, Z. Huang, K. Song, J. Liu, J. Troughton, N. Gasparini, C. Zhou, Y. Lin, D.-J. Xue, B. Chen, A. K. Johnston, N. Wei, M. N. Hedhili, M. Wei, A. Y. Alsalloum, P. Maity, B. Turedi, C. Yang, D. Baran, T. D. Anthopoulos, Y. Han, Z.-H. Lu, O. F. Mohammed, F. Gao, E. H. Sargent, O. M. Bakr, *Nat. Energy* **2020**, *5*, 131.
[7] Q. Wang, N. Phung, D. Di Girolamo, P. Vivo, A. Abate, *Energy Environ. Sci.* **2019**, *12*, 865.
[8] L. Meng, J. You, T.-F. Guo, Y. Yang, *Acc. Chem. Res.* **2016**, *49*, 155.
[9] D.-N. Jeong, J.-M. Yang, N.-G. Park, *Nanotechnology* **2020**, *31*, 152001.
[10] G. M. Paternò, V. Robbiano, L. Santarelli, A. Zampetti, C. Cazzaniga, V. Garcìa Sakai, F. Cacialli, *Sustainable Energy Fuels* **2019**, *3*, 2561.
[11] F. Lang, M. Jošt, J. Bundesmann, A. Denker, S. Albrecht, G. Landi, H.-C. Neitzert, J. Rappich, N. H. Nickel, *Energy Environ. Sci.* **2019**, *12*, 1634.
[12] A. Dubey, N. Adhikari, S. Mabrouk, F. Wu, K. Chen, S. Yang, Q. Qiao, *J. Mater. Chem. A* **2018**, *6*, 2406.
[13] L. K. Ono, Y. Qi, S. Liu, *Joule* **2018**, *2*, 1961.
[14] M. Saliba, M. Stolterfoht, C. M. Wolff, D. Neher, A. Abate, *Joule* **2018**, *2*, 1019.
[15] J. Yang, B. D. Siempelkamp, D. Liu, T. L. Kelly, *ACS Nano* **2015**, *9*, 1955.
[16] J. A. Christians, P. A. Miranda Herrera, P. V. Kamat, *J. Am. Chem. Soc.* **2015**, *137*, 1530.
[17] A. J. Pearson, G. E. Eperon, P. E. Hopkinson, S. N. Habisreutinger, J. T.-W. Wang, H. J. Snaith, N. C. Greenham, *Adv. Energy Mater.* **2016**, *6*, 1600014.
[18] B.-w. Park, S. I. Seok, *Adv. Mater.* **2019**, *31*, 1805337.
[19] B. Conings, J. Drijkoningen, N. Gauquelin, A. Babayigit, J. D'Haen, L. D'Olieslaeger, A. Ethirajan, J. Verbeeck, J. Manca, E. Mosconi, F. D. Angelis, H.-G. Boyen, *Adv. Energy Mater.* **2015**, *5*, 1500477.
[20] E. T. Hoke, D. J. Slotcavage, E. R. Dohner, A. R. Bowring, H. I. Karunadasa, M. D. McGehee, *Chem. Sci.* **2015**, *6*, 613.
[21] K. Domanski, B. Roose, T. Matsui, M. Saliba, S.-H. Turren-Cruz, J.-P. Correa-Baena, C. R. Carmona, G. Richardson, J. M. Foster, F. De Angelis, J. M. Ball, A. Petrozza, N. Mine, M. K. Nazeeruddin, W. Tress, M. Grätzel, U. Steiner, A. Hagfeldt, A. Abate, *Energy Environ. Sci.* **2017**, *10*, 604.
[22] A. F. Akbulatov, L. A. Frolova, M. P. Griffin, I. R. Gearba, A. Dolocan, D. A. Vanden Bout, S. Tsarev, E. A. Katz, A. F. Shestakov, K. J. Stevenson, P. A. Troshin, *Adv. Energy Mater.* **2017**, *7*, 1700476.
[23] X. Li, S. Fu, S. Liu, Y. Wu, W. Zhang, W. Song, J. Fang, *Nano Energy* **2019**, *64*, 103962.
[24] A. Guerrero, J. You, C. Aranda, Y. S. Kang, G. Garcia-Belmonte, H. Zhou, J. Bisquert, Y. Yang, *ACS Nano* **2016**, *10*, 218.
[25] G. Y. Kim, A. Senocrate, T.-Y. Yang, G. Gregori, M. Grätzel, J. Maier, *Nat. Mater.* **2018**, *17*, 445.
[26] Z. Huang, X. Hu, C. Liu, X. Meng, Z. Huang, J. Yang, X. Duan, J. Long, Z. Zhao, L. Tan, Y. Song, Y. Chen, *Adv. Funct. Mater.* **2019**, *29*, 1902629.
[27] S. Wang, H. Chen, J. Zhang, G. Xu, W. Chen, R. Xue, M. Zhang, Y. Li, Y. Li, *Adv. Mater.* **2019**, *31*, 1903691.
[28] H. Zhao, S. Yang, Y. Han, S. Yuan, H. Jiang, C. Duan, Z. Liu, S. Liu, *Adv. Mater. Technol.* **2019**, *4*, 1900311.
[29] S. Fu, W. Zhang, X. Li, L. Wan, Y. Wu, L. Chen, X. Liu, J. Fang, *ACS Energy Lett.* **2020**, *5*, 676.
[30] A. Uddin, B. M. Upama, H. Yi, L. Duan, *Coatings* **2019**, *9*.
[31] K. Domanski, J.-P. Correa-Baena, N. Mine, M. K. Nazeeruddin, A. Abate, M. Saliba, W. Tress, A. Hagfeldt, M. Grätzel, *ACS Nano* **2016**, *10*, 6306.
[32] S. Cacovich, L. Ciná, F. Matteocci, G. Divitini, P. A. Midgley, A. Di Carlo, C. Ducati, *Nanoscale* **2017**, *9*, 4700.
[33] A. K. M M. V. Khenkin, E. A. Katz, I. Visoly-Fisher, *Energy Environ. Sci.* **2019**, *12*, 550.
[34] Q. Jeangros, M. Duchamp, J. Werner, M. Kruth, R. E. Dunin-Borkowski, B. Niesen, C. Ballif, A. Hessler-Wyser, *Nano Lett.* **2016**, *16*, 7013.

[35] K. Han, M. Xie, L. Zhang, L. Yan, J. Wei, G. Ji, Q. Luo, J. Lin, Y. Hao, C.-Q. Ma, *Sol. Energy Mater. Sol. Cells* **2018**, *185*, 399.
[36] M. Wang, H. Wang, W. Li, X. Hu, K. Sun, Z. Zang, *J. Mater. Chem. A* **2019**, *7*, 26421.
[37] H. Lee, C. Lee, *Adv. Energy Mater.* **2018**, *8*, 1702197.
[38] National Institutes of Health, Source Software, https://imagej.nih.gov/ij/, (accessed March 2020).
[39] N. Li, S. Tao, Y. Chen, X. Niu, C. K. Onwudinanti, C. Hu, Z. Qiu, Z. Xu, G. Zheng, L. Wang, Y. Zhang, L. Li, H. Liu, Y. Lun, J. Hong, X. Wang, Y. Liu, H. Xie, Y. Gao, Y. Bai, S. Yang, G. Brocks, Q. Chen, H. Zhou, *Nat. Energy* **2019**, *4*, 408.
[40] S. Zuo, X. Zhu, J. Feng, Z. Wang, C. Zhang, C. Wang, X. Ren, S. Liu, D. Yang, *Sol. RRL* **2019**, *3*, 1900207.
[41] W. Qiu, M. Buffière, G. Brammertz, U. W. Paetzold, L. Froyen, P. Heremans, D. Cheyns, *Org. Electron.* **2015**, *26*, 30.
[42] B. Chen, J. Song, X. Dai, Y. Liu, P. N. Rudd, X. Hong, J. Huang, *Adv. Mater.* **2019**, *31*, 1902413.
[43] K. Domanski, E. A. Alharbi, A. Hagfeldt, M. Grätzel, W. Tress, *Nat. Energy* **2018**, *3*, 61.
[44] L. Yan, J. Yi, Q. Chen, J. Dou, Y. Yang, X. Liu, L. Chen, C.-Q. Ma, *J. Mater. Chem. A* **2017**, *5*, 10010.
[45] J. Xiong, B. Yang, C. Cao, R. Wu, Y. Huang, J. Sun, J. Zhang, C. Liu, S. Tao, Y. Gao, J. Yang, *Org. Electron.* **2016**, *30*, 30.
[46] Y. Wang, S. Wang, X. Chen, Z. Li, J. Wang, T. Li, X. Deng, *J. Mater. Chem. A* **2018**, *6*, 4860.
[47] A. P. Kulkarni, C. J. Tonzola, A. Babel, S. A. Jenekhe, *Chem. Mater.* **2004**, *16*, 4556.
[48] N. Shibayama, H. Kanda, T. W. Kim, H. Segawa, S. Ito, *APL Mater.* **2019**, *7*, 031117.
[49] C. Chen, S. Zhang, S. Wu, W. Zhang, H. Zhu, Z. Xiong, Y. Zhang, W. Chen, *RSC Adv.* **2017**, *7*, 35819.
[50] S. A. Gevorgyan, M. V. Madsen, B. Roth, M. Corazza, M. Hösel, R. R. Søndergaard, M. Jørgensen, F. C. Krebs, *Adv. Energy Mater.* **2016**, *6*, 1501208.
[51] D. C. Johnston, *Phys. Rev. B* **2006**, *74*, 184430.
[52] M. V. Khenkin, E. A. Katz, A. Abate, G. Bardizza, J. J. Berry, C. Brabec, F. Brunetti, V. Bulović, Q. Burlingame, A. Di Carlo, R. Cheacharoen, Y.-B. Cheng, A. Colsmann, S. Cros, K. Domanski, M. Dusza, C. J. Fell, S. R. Forrest, Y. Galagan, D. Di Girolamo, M. Grätzel, A. Hagfeldt, E. von Hauff, H. Hoppe, J. Kettle, H. Köbler, M. S. Leite, S. Liu, Y.-L. Loo, J. M. Luther, et al., *Nat. Energy* **2020**, *5*, 35.